X-ray studies of the surface and bulk structure of the isotropic and nematic phase of a lyotropic liquid crystal

G. Swislow, D. Schwartz, B. M. Ocko,* and P. S. Pershan
Department of Physics and the Division of Applied Science, Harvard University, Cambridge, Massachusetts 02138

J. D. Litster
Department of Physics, Massachusetts Institute of Technology, Cambridge, Massachusetts 02139
(Received 30 July 1990; revised manuscript received 4 February 1991)

We have used x-ray specular reflection to study the structure of the air–liquid-crystal interface of the lyotropic liquid crystal formed from binary mixtures of cesium perfluoro-octanoate (CsPFO) and water. In the isotropic phase the surface is coated with a monolayer of CsPFO separated by layers of water from one or more smectic bilayers of CsPFO. As for the case of thermotropic liquid crystals, the isotropic-to-nematic phase transition has no effect on the surface structure, and as the temperature is lowered towards the nematic–to–smectic-A transition temperature, the number of surface-induced smectic layers increases dramatically (e.g., approximately 100 layers were observed). Theoretical modeling of the reflectivity excludes the possibility that the surface bilayers are arrays of micelles. X-ray scattering from critical smectic short-range order in the bulk, studied by tuning the spectrometer away from the specular condition, indicates that the scattering is fundamentally different from short-range smectic order in thermotropic systems.

INTRODUCTION

A major incentive for the study of phase transitions in liquid crystals is the belief that systems whose macroscopic observables have the same symmetry should display similar, or universal, critical behavior, independent of their microscopic, or molecular properties.[1–4] The critical, and near-critical, properties in the vicinity of the phase transition between the nematic and smectic-A phases have been extensively studied in this context. Most of this work has been done on single-component systems in which the liquid-crystalline phase transitions occur as a function of temperature, i.e., thermotropic liquid crystals. Although some of these measurements agree with the de Gennes–McMillan Landau model of the nematic–to–smectic-A phase transition, the existing models have not been able to explain all of the observed features.

More recently, nematic and smectic-A liquid-crystalline phases have been identified in two- and three-component systems in which the stable phases appear to be made up of small anisotropic molecular aggregates, or micelles.[5,6] Since water is commonly one of these chemical components, these systems are broadly referred to as "lyotropic." To a first approximation, the micelles are ellipsoids of revolution that can have either the prolate or the oblate form. It is not clear whether the transition from the nematic to smectic-A phase involves an ordering of the anisotropic micelles, or whether there is a microscopic transformation in which the micelles aggregate into a lamellar structure similar to the L_α phase observed in lecithins and other surfactants.[7] Since phases of lyotopic systems have the same macroscopic symmetry as those of thermotropic systems, but with very different interparticle interactions, a comparison of properties of the two systems may be useful in developing new insights into the fundamental nature of the nematic–to–smectic-A (N–Sm-A) transition.[8]

The binary system of cesium perfluoro-octanoate in water (CsPFO), investigated by Boden *et al.*, has been extensively studied by a variety of techniques.[9] One of its main advantages as a model system is that it exhibits liquid-crystal phases over a wide range of concentrations. This is in contrast to most other micellar systems, in which the liquid-crystalline phases occur only in mixtures containing a third component, often an alcohol or "cosurfactant," and over a limited range of concentrations.[6,7] The phase diagram for the CsPFO-H_2O system[10] is reproduced in Fig. 1. At the highest temperatures the system forms an isotropic micellar phase which first transforms on lowering the temperature into a nematic phase and, upon further cooling, into a smectic-A phase. On the basis of nuclear-magnetic-resonance (NMR) studies of the orientation of D_2O, Boden *et al.*[9] conclude that the nematic phase of CsPFO-D_2O solutions consists of oblate micelles in which the ionic groups on the outside shield the interior fluorocarbons from the D_2O. They estimate that the ratio of major to minor diameters is about 3 to 5. For all the D_2O concentrations reported in this phase diagram the temperature range of the nematic phase is about 7 °C.

For concentrations exceeding approximately 42% by weight of water, NMR,[11] light scattering,[12] magnetic susceptibility,[13] and x-ray scattering[14] studies indicate that the nematic–to–smectic-A transition is accompanied by very large pretransition effects, strongly suggesting a second-order transition. According to the phase diagram shown in Fig. 1, there is a tricritical point at approxi-

 ©1991 The American Physical Society

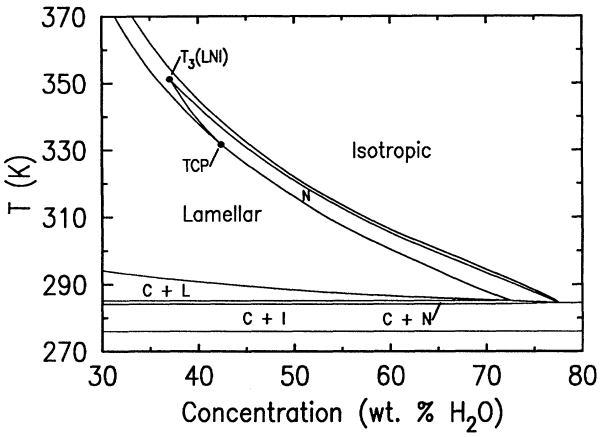

FIG. 1. Phase diagram of solutions of CsPFO and H_2O from Ref. 9.

mately 42% by weight H_2O, and for lower water content the transition is first order. On the basis of electrical conductivity studies, Boden *et al.*[14] suggest there is not a dramatic change in either the size or the shape of the micelles at the nematic–to–smectic-A transition; however, on the basis of x-ray scattering studies they argue that there is a significant change within the smectic-A phase.[10]

In the first paper describing the liquid-crystalline phases of CsPFO solutions Boden *et al.*[9] demonstrated that the nematic phase of CsPFO could be aligned by an external magnetic field. Unfortunately, the observed x-ray patterns[14] suggest that the magnetically induced alignment is not as complete as in thermotropic systems.[15] This is, in part, a consequence of the fact that the anisotropy in the diamagnetic susceptibility of the CsPFO micelle is significantly smaller than that of most thermotropic liquid-crystal molecules. As a result, it has been difficult to carry out quantitative x-ray measurements of the bulk critical properties of the nematic–to–smectic-A transition of CsPFO. Recent experiments on thermotropic systems, using a free-surface geometry, have demonstrated that in both the nematic and isotropic phases the free surface induces nearly perfect orientational alignment of the bulk nematic phase below the surface.[16–18] One of the purposes of this paper is to describe results on the critical properties of the nematic phase of CsPFO-H_2O solutions in which the director is relatively well aligned by such a free surface. Unfortunately, small amounts of H_2O that were lost by evaporation on passing through the nematic–to–smectic-A transition caused minute changes in concentration. Since this made it difficult to locate $T_{N-\text{Sm-}A}$ precisely, the results on the critical properties are only semiquantitative. Nevertheless, we will present results demonstrating that critical diffuse scattering from the bulk nematic phase below the surface is qualitatively different from critical diffuse scattering in the nematic phase of thermotropic systems.

A second purpose of this article is to present x-ray specular reflection results from the free surface of CsPFO-H_2O solutions as a function of temperature in both the isotropic and nematic phases. These measurements unambiguously demonstrate that there is smectic order at the surface for temperatures at which the bulk phase is isotropic. Detailed analysis of the data suggests that the surface is coated with a monolayer of CsPFO which is separated from *subsurface* layers of CsPFO by a layer of water. In the nematic phase, as $T_{N-\text{Sm-}A}$ is approached from above, the number of coherent surface layers increases[19] to approximately 100.

SAMPLE PROPERTIES

The present experiments were carried out on samples of between 50% and 60% H_2O by weight. They were prepared by pipetting approximately 2 ml of solution onto a 76.2-mm-diam glass substrate that was mounted in a sealed temperature-controlled sample cell.[20] According to Boden *et al.*[9] $T_{N-\text{Sm-}A} \approx 30\,^{\circ}\text{C}$ and $T_{N-I} \approx 37\,^{\circ}\text{C}$ for concentrations of approximately 60 wt. % H_2O. Both transition temperatures increase by about 1.2 °C for each 1% decrease in H_2O concentration. Consequently, evaporative losses of only 0.016 ml of H_2O (approximately 0.8% by volume) are sufficient to increase the transition temperatures by 1 °C. Since this was typical of the variations that occurred whenever the sealed cell was opened to the laboratory atmosphere, it was not possible to preselect the transition temperature for a given sample to better than 1 °C.

The sample cell consisted of inner and outer cans whose temperature could be controlled independently. The windows of both cans were Kapton. In order to maintain the necessary temperature homogeneity of the inner cell these windows were coated with several hundred angstroms of gold. The temperature of the glass substrate was cooled approximately 1 °C below the rest of the cell by a thermoelectric device to minimize condensation of water elsewhere. The region between the substrate and the thermoelectric device was coated by a thin layer of silicon vacuum grease.

X-RAY CONSIDERATIONS

The x-ray experiments were carried out at the National Synchrotron Light Source on beam line X22b. The general features of x-ray reflectometers capable of measuring specular reflectivity from a horizontal liquid surface have been described elsewhere.[21,22] The present liquid spectrometer utilized two Ge(111) crystals. The first crystal monochromatized the incident beam ($\lambda = 1.710$ Å) and the second crystal was tilted to deflect the incident beam downward to achieve the desired incident angle α with the surface. The sample is lowered by the amount necessary to intercept the incident beam.

Figure 2 illustrates the kinematics of the reflectometer. Following the second Ge(111) crystal, the beam makes a vertical angle α with the horizontal. The distance L between the second monochromator and the center of the

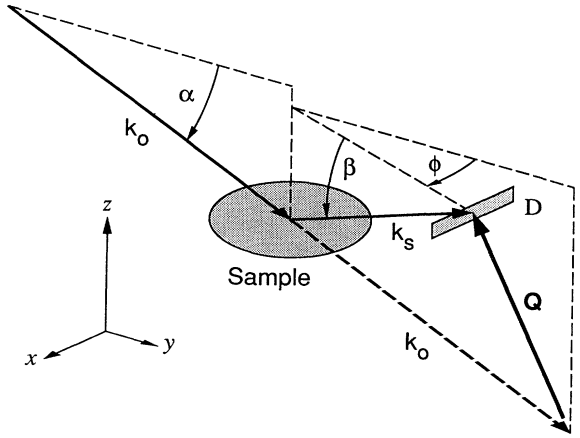

FIG. 2. Kinematics of the liquid surface reflectometer following *the second monochromator* as discussed in the text. The beam $\mathbf{k}_0$ incident on the sample at an angle α from the horizontal strikes it at a horizontal distance L, and a vertical distance $h=L\tan(\alpha)$ from the center of the monochromator. The detector D is located at a horizontal distance L from the center of the sample, at a horizontal angle ϕ from the plane of incidence. It can be raised or lowered such that the vertical angle between the detected radiation and the horizontal is β. The vertical displacement of the detector is $L[\tan(\beta)-\tan(\alpha)]$. For specular reflection $\alpha=\beta$.

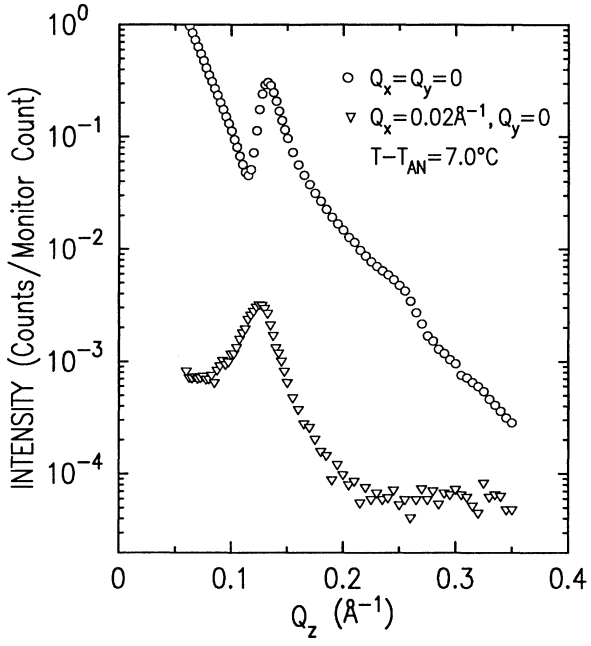

FIG. 3. X-ray scattering intensity as a function of Q_z through the points $Q_y=0$ with $Q_x=0.0$ Å^{-1}(○) and $Q_x=0.02$ Å^{-1}(△) for $T-T_{N-\mathrm{Sm}-A}=7.0$°C. The difference between the two scans is interpreted as the specular reflection.

sample is approximately equal to 650 mm and the sample is mounted on an elevator that maintains $h=L\tan(\alpha)$.[23] The incident beam is defined by a slit just before the sample. A detector slit D, followed by a Na(I) scintillation detector, is mounted at the end of an output arm an equal distance L from the sample. The vertical angle β and the horizontal angle ϕ can be adjusted independently to select the wave-vector transfer $\mathbf{Q}$ between the incident and scattered wave. Taking $k_0\equiv(2\pi/\lambda)$,

$$\begin{aligned} Q_x/k_0&=\cos(\beta)\sin(\phi)\ ,\\ Q_y/k_0&=\cos(\beta)\cos(\phi)-\cos(\alpha)\ ,\\ Q_z/k_0&=\sin(\beta)+\sin(\alpha)\ . \end{aligned} \tag{1}$$

Neglecting the small angular divergence of the incident beam, the resolution of reflectometer for *diffuse scattering* is primarily determined by L and the size of the detector slit. Near the specular condition $\alpha=\beta$ and $\phi=0$, the corresponding full widths at half maximum are $\Delta Q_z=0.01$ Å^{-1}, $\Delta Q_x=0.03$ Å^{-1}, and $\Delta Q_y=\sin(\alpha)\Delta Q_z$. Typically $\alpha\leq 1°\lesssim\sim 1.5°$ and $\Delta Q_y\leq(1.65\sim 2.6)\times 10^{-4}$ Å^{-1}. Since the physical condition for specular reflection requires $\beta=\alpha$, the zy resolution appropriate to specular reflection $\Delta Q_{z,y}^{(\mathrm{surf})}$ is primarily determined by the angular spread of the incident beam and the flatness of the surface. As the resolution appropriate to diffuse scattering ΔQ_z depends on the angular acceptance of the detector, it was typically more than ten times larger than $\Delta Q_{z,y}^{(\mathrm{surf})}$. The transverse resolution ΔQ_x is the same for both specular and diffuse scattering.

The intensity measured when the reflectometer is set to the specular condition is the superposition of specular reflectivity and critical diffuse scattering from the bulk. Fortunately, near the specular condition the diffuse scattering $S(\mathbf{Q})$ is usually a slowly varying function of Q_x and Q_y and can be separated from the specular reflection by detuning the reflectometer slightly from the specular condition along either Q_x or Q_y. The specular signal is obtained as the difference between the signals measured at the specular condition and the detuned condition. Figure 3 shows the measured intensity for scans along Q_z with $Q_x=Q_y=0$ (○) and an os-scan in which $Q_x=0.02$ Å^{-1} and $Q_y=0$ (▽) for $T-T_{N-\mathrm{Sm}-A}=7.0$°C ($T<T_{I-\mathrm{Sm}-A}$).

EXPERIMENTAL RESULTS

We have measured both the specular reflection $R(Q_z)$ from the surface and diffuse scattering $S(\mathbf{Q})$ from the bulk as a function of temperature for a mixture of CsPFO and 58% H_2O by weight. The specular reflection signal, divided by the theoretical Fresnel reflectivity for an ideal flat surface,[24] $R(Q_z)/R_F(Q_z)$, is shown in Fig. 4 as open circles for five temperatures within the nematic phase and one temperature 35.84 °C in the isotropic phase.[14] Since the nematic–to–smectic-A transition temperature for this sample is approximately 28 °C, none of these data are

very close to the transition temperature.[25]

A feature common to the present CsPFO reflectivity profiles and previous ones taken on thermotropic liquid-crystal systems is a peak at $Q_z \approx 2\pi/D$, where D is the smectic repeat distance. Since D for this concentration of CsPFO is known to be approximately 50 Å (corresponding to a peak at $2\pi/50$ Å$=0.1256$ Å^{-1}), the first peak must arise from surface-induced smectic layering.[14] The weaker peaks at the second-harmonic positions are typically not observed in thermotropic systems except when there is strong competition between monolayer and bilayer smectic ordering.[26] Interference between reflections from the smectic layers and reflection from the liquid-vapor interface produces asymmetries in the reflectivity profiles. For the CsPFO system, as seen in Fig. 4, there is always a dip before the first peak. In contrast, this asymmetry is reversed for thermotropic liquid crystals.

In all cases in which the free-surface geometry has been used for thermotropic nematic–liquid-crystal measurements, the surface-induced smectic order induced full homogeneous alignment of the director in the bulk phase below the surface, i.e., along the surface normal.[16,17,27] Figure 5(a) illustrates the diffuse x-ray scattering distributions $S(\mathbf{Q})$ typical of the thermotropic nematic phase in

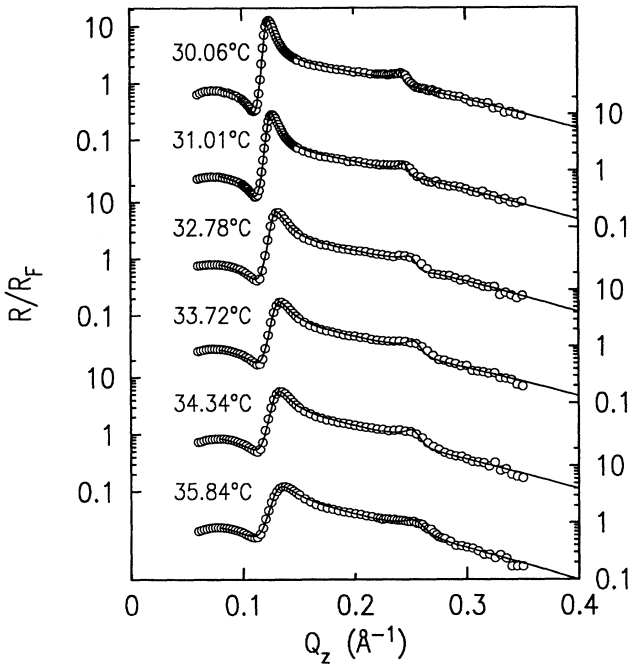

FIG. 4. Normalized specular reflectivity results $R(Q_z)/R_F(Q_z)$ for five different temperatures in a CsPFO solution containing 58% H_2O by weight. The temperatures, from top to bottom, are five in the nematic phase, 30.06 °C, 31.01 °C, 32.78 °C, 33.72 °C, 34.34 °C, and one in the isotropic phase, 35.84 °C. The nematic–to–smectic-A transition temperature is approximately 28 °C. The solid line through the data illustrates the reflected intensity predicted by a model of the surface that is discussed in the text, Eq. (2) with $\Phi(Q)$ given by Eq. (8).

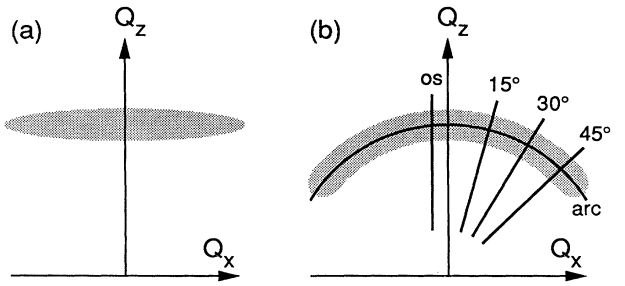

FIG. 5. (a) Schematic illustration of typical diffuse scattering observed from the nematic phase of thermotropic liquid crystals. (b) Schematic illustration of the diffuse scattering from the bulk of CsPFO and the five scans used in measuring it: arc scan $Q_y = 6\times10^{-4}$ Å^{-1}, $Q_x^2+Q_z^2=Q_0^2\approx(0.125$ Å$^{-1})^2$; os scan $Q_y=0$, $Q_x=0.02$ Å^{-1}, and radial scans at $Q_x/Q_z=\tan(\chi)$ for $\chi=15°$, 30°, and 45°, respectively.

both the present reflection geometry and in a transmission geometry in which the director is aligned by an external magnetic field along the z direction.[28] The intensity is distributed in reciprocal space as a flat ellipsoid whose minor axis is along the director. On cooling towards $T_{N-\text{Sm-}A}$ the ellipsoid condenses around $Q_z=2\pi/D$ and the reciprocals of the half widths along and perpendicular to z define the correlation lengths $\xi_\parallel$ and $\xi_\perp$, respectively. In the present studies of CsPFO we find that the diffuse scattering from the bulk differs from that of thermotropic phases in the following way: instead of being distributed as a flat ellipsoid, it is distributed along a nearly spherical surface. The intersection of that surface with the Q_x-Q_z plane is illustrated in Fig. 5(b). As in the thermotropic case, on cooling towards $T_{N-\text{Sm-}A}$ the intensity condenses at $Q_z=2\pi/D$. The data in Fig. 6 illustrate this for CsPFO at three temperatures.

Data from the os scan are shown, as ▽ in Fig. 3. Since the width of the arc scans is significantly broader than 15° for most of the temperatures studied, there is little difference between the os scan at $Q_x=0.02$ Å^{-1} and the 15° radial scan whose peaks correspond to $Q_x=(0.125$ Å$^{-1})\times\tan(15°)=0.003$ Å^{-1}. In Fig. 6 we present results for the arc scan, and radial scans at 15°, 30°, and 45°. Figure 6 shows data for $T=30.06$ °C, 32.78 °C, and 35.84 °C. The first two temperatures are in the nematic phase and the highest is in the isotropic phase. The sketch in Fig. 5(b) was motivated by the anticipation of the observation that the radial scans in Fig. 6 are all peaked at approximately 0.125 Å^{-1}. The scans were all taken at a small offset $Q_y\approx0.0006$ Å^{-1} to minimize the effects of the much stronger specular reflection at $Q_y=0$. The sharp resolution limited peaks at $Q_x=0$ in the arc scans of Fig. 6 are a remnant of the specular reflectivity. For lower temperatures, the diffuse intensity condenses around $Q_x=Q_y=0$, $Q_z\approx0.125$ Å^{-1}, and the separation between the sharp central peak and the diffuse background is subtle; however, the shape of the central peak is well charac-

terized and it can be separated quantitatively. The arrows in the Fig. 6 arc scans indicate the positions where the radial scans cross the arc.

Except for the central peak originating from the specular reflectivity, the intensity distribution along the arc scan in Fig. 6 for the isotropic phase is nearly constant. We cannot be certain whether the slight variation is due to the bulk scattering function $S(\mathbf{Q})$ or whether the geometry of the reflectometer gives rise to this variation. In the nematic phase, local smectic fluctuations induce excess diffuse scattering above what is present in the isotropic phase. By measuring the intensity of the diffuse scattering at $Q_z = 0.125$ Å^{-1}, $Q_y = 0$, and $Q_x = 0.02$ Å^{-1}, the isotropic to nematic transition temperature can be determined. This is illustrated by the data in Fig. 7, which were obtained at this $\mathbf{Q}$ vector while cooling the sample at a rate of approximately 4 °C per hour. The intensity, essentially constant above 34.5 °C, increases dramatically below that temperature, indicating the onset of critical bulk scattering.

Finally, we would like to emphasize that all of the variations that we have described, in both the bulk and specular results, are reversible as long as the sample is not cooled below $T_{N-\mathrm{Sm}\text{-}A}$. Furthermore, even if the sample is cooled below $T_{N-\mathrm{Sm}\text{-}A}$ the results are also reproducible on heating the sample up into the isotropic phase and then recooling. We thus rule out the possibility that intensity distribution along the arc is due to a nonequilibrium mosaic distribution of nematic directors as was observed in some of the earliest experiments on partially aligned thermotropic nematic phases.[29]

ANALYSIS OF SPECULAR REFLECTIVITY

In the limit that $Q_z \gg Q_c$ the theoretical expression for $R(Q_z)/R_F(Q_z)$ can be expressed in terms of the derivative of the average electron density $\langle \rho(z) \rangle$ at any height z along the surface normal:[16,30]

$$\frac{R(Q_z)}{R_F(Q_z)} = \left| \frac{1}{\rho_\infty} \int_{-\infty}^{\infty} \frac{\partial \langle \rho(z) \rangle}{\partial z} e^{iQ_z z} dz \right|^2 \equiv |\Phi(Q_z)|^2 . \quad (2)$$

In the absence of the theoretical guidance our attempts to model the observed data for $R(Q_z)/R_F(Q_z)$ are somewhat empirical. However, guided by the fact that peaks observed in $R(Q_z)/R_F(Q_z)$ mean that the surface imposes a density modulation which decays with distance from the bulk, we tried two simple models. Both were able to represent the data satisfactorily, and hence are

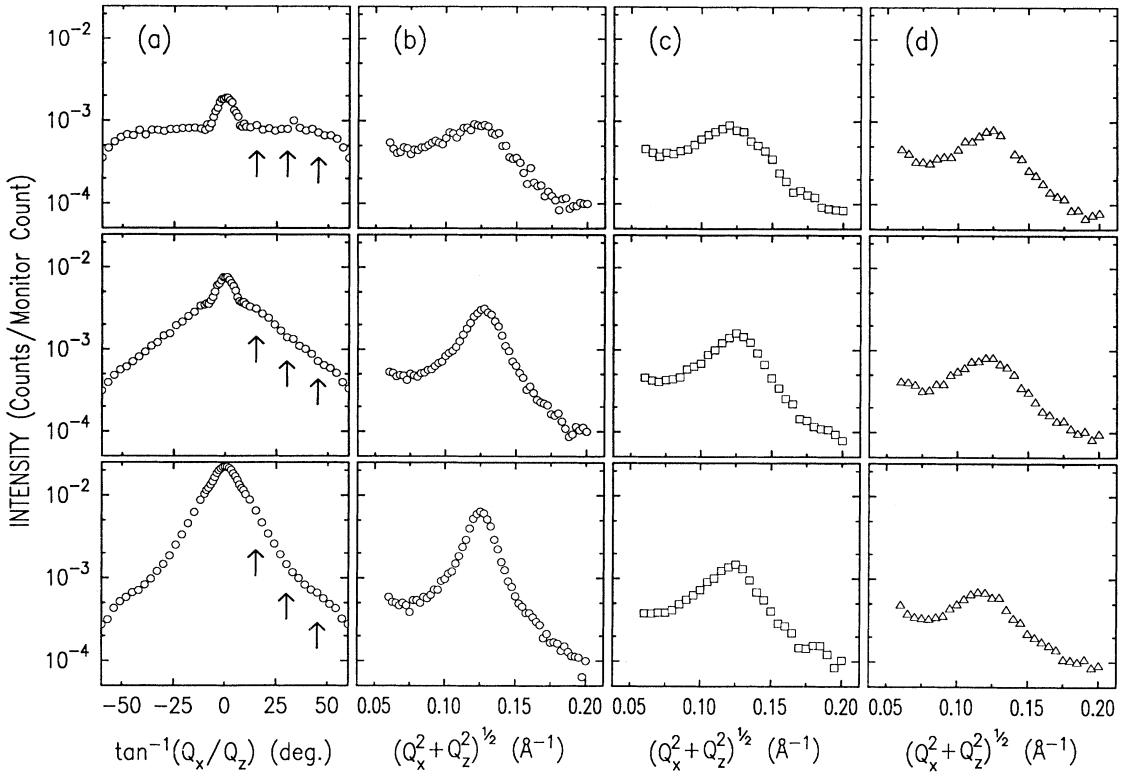

FIG. 6. Diffuse scattering from the bulk of CsPFO; the scans are described in Fig. 5(b). The left column (a) shows arc scans at $T = 35.84$ °C, 32.78 °C, and 30.06 °C from top to bottom. The three remaining columns show radial scans, at the same temperatures, of type (b) 15°, (c) 30°, and (d) 45°. For most temperatures the os scan illustrated in Fig. 5(b) is indistinguishable from the 15° radial scan.

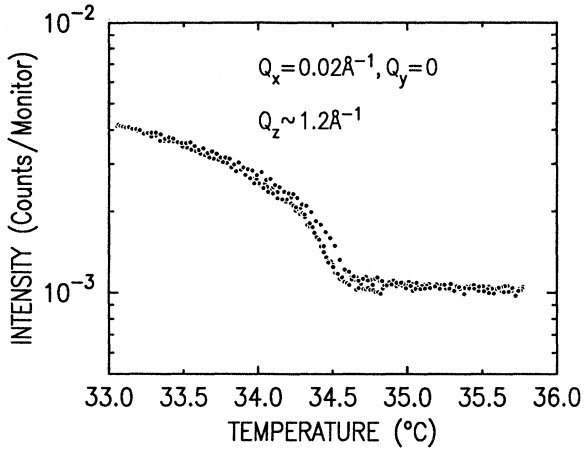

FIG. 7. Diffuse scattering as a function of temperature from bulk CsPFO at $Q_z=0.125$ Å^{-1}, $Q_y=0$, and $Q_x=0.02$ Å^{-1}.

not unique: however, both have certain features in common, which are likely to be there for any successful model and therefore give a reasonable indication of the surface structure of the sample.

One feature common to both models was an expression to describe the increase in $\langle\rho(z)\rangle$ from zero for $z\geq 0$, above the surface, to the bulk value ρ_∞, far below the surface. For simple liquids a form of the type $\rho_\infty[1-\mathrm{erf}(z/\sigma)]/2$ has proven adequate. However, fits to the present data are significantly improved if the expression used for electron density near the surface first rises to a value that is larger than ρ_∞ before decaying to ρ_∞. Consequently, we have modeled the near surface region with a form that, near $z\cong 0$, first rises to a value of $(1+A_0)\rho_\infty$ over a range of $\Delta z\cong\sigma_{s1}$ and then, over a region $\Delta z\cong\sigma_{s2}$, decays to ρ_∞:

$$\left.\frac{\langle\rho(z)\rangle}{\rho_\infty}\right|_S=(1+A_0)\frac{[1-\mathrm{erf}(z/\sigma_{s1})]}{2}-A_0\frac{\{1-\mathrm{erf}[(z-d_0)/\sigma_{s2}]\}}{2}\ . \tag{3}$$

The two models differ in how we represent the layered structure. The first one assumes the surface imposed layering can be represented by an electron density variation having the form

$$\left.\frac{\langle\rho(z)\rangle}{\rho_\infty}\right|_L=A_1\sum_{n=0}^{\infty}\Gamma(z-d_s-nd)e^{-nd/\xi}\ , \tag{4}$$

where $\Gamma(z)$ models the z dependence of the averaged form factor for the structure of an individual layer (i.e., the layer form factor). The first layer is centered at $z=d_s d_s$ and the amplitude of successive layers, separated by $\Delta z=d$, decays as $\exp(nd/\xi)$. Since $\Gamma(z)$ describes deviations between the average electron density in the bulk ρ_∞ and the local density averaged over a plane at constant z, $\langle\rho(z)\rangle$, the model must have the property that $\int\Gamma(z)dz=0$. Thus we take

$$\Gamma(g)=\left[g(z)-\frac{g(z-d_I)}{2}-\frac{g(z+d_I)}{2}\right], \tag{5}$$

where

$$g(z)=\frac{1}{(2\pi\sigma_I^2)^{1/2}}e^{-z^2/2\sigma_I^2}\ . \tag{6}$$

The form of $\Phi(Q_z)$ may be calculated from the sum of Eqs. (3) and (4)

$$\frac{\langle\rho(z)\rangle}{\rho_\infty}=\left.\frac{\langle\rho(z)\rangle}{\rho_\infty}\right|_S+\left.\frac{\langle\rho(z)\rangle}{\rho_\infty}\right|_L, \tag{7}$$

which is

$$\Phi(Q)=(1+A_0)e^{-Q^2\sigma_{s1}^2/2}-A_0e^{-Q^2\sigma_{s2}^2/2}e^{iQd_0}-2iA_1Q\sin^2(Qd_I/2)\times e^{-Q^2(\sigma_{s1}^2+\sigma_I^2)/2}e^{iQd_s}\left[\frac{1}{(1-\phi)}\right], \tag{8}$$

where $\phi=e^{-d/\xi+iQd}$. Although this model has ten parameters, which seems to be a lot, it has to describe a fairly complicated surface structure. As we will indicate below, the significant physical result is not the particular values of the parameters, but rather those features of the model surface profile which are insensitive to the details of the model.

The solid lines in Fig. 4 represent fits[31] of the data to the form for $R(Q_z)/R_F(Q_z)$, which is obtained on substitution of this result into Eq. (2) (see Table I). Figure 8 displays the near surface structure of $\langle\rho(z)\rangle/\rho_\infty$ for these fits. The horizontal lines in Fig. 8 indicate the electron density of Teflon (—CF_2—CF_2—), $1.46\rho_\infty$, and the electron density of H_2O, $0.8\rho_\infty$.[32] The first thing to note about this model for the electron density is that the width

TABLE I. Parameters obtained by fitting the data of Fig. 4 to Eq. (2) with $\Phi(Q)$ given by Eq. (8).

T (°C)	A_0	σ_1 (Å)	σ_1 (Å)	d_0 (Å)	A_1	d (Å)	d_s (Å)	d_1 (Å)	σ_1 (Å)	ξ (Å)
35.84	1.27	11.19	4.20	9.76	−88.8	49.5	16.6	4.64	4.79	89.2
34.34	1.19	10.36	4.00	9.70	−78.0	49.7	18.1	5.09	6.82	118.3
33.72	1.21	10.02	3.89	9.53	−69.6	49.4	17.9	5.47	7.48	126.3
32.78	1.25	9.37	4.06	8.50	−59.6	50.0	18.5	6.28	9.22	145.6
31.01	1.40	10.38	4.08	8.72	−61.6	51.4	17.5	6.53	9.00	220.7
30.06	1.49	10.65	4.08	8.64	−67.6	52.4	17.1	6.53	9.00	258.7

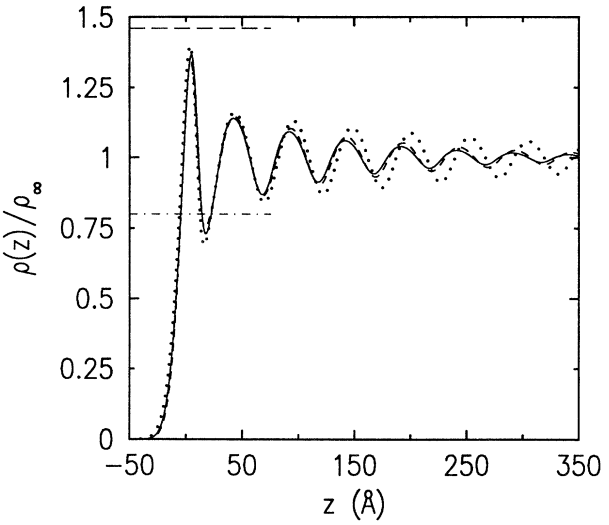

FIG. 8. Electron density profiles $\langle\rho(z)\rangle/\rho_\infty$ corresponding to the fits shown in Fig. 4 for $T=35.84\,^\circ$C (——), 32.78 °C (— — —), and 30.06 °C (· · · ·). The horizontal lines indicate at 1.46 the electron density of Teflon, and at 0.80 the electron density of H_2O.

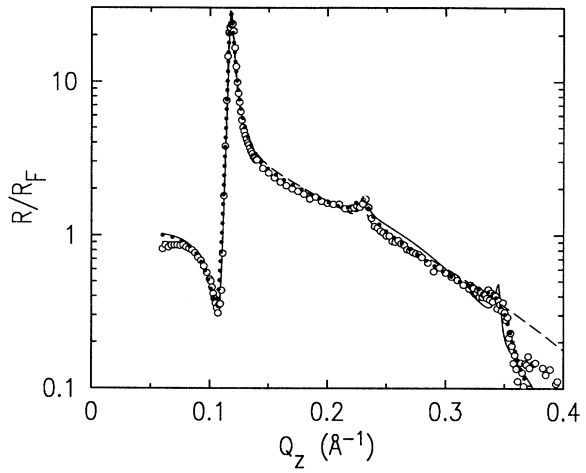

FIG. 9. Normalized specular reflectivity results for $R(Q_z)/R_F(Q_z)$ at $T-T_{N-\text{Sm-}A}$ approximately 1.6 °C that show structure at the third-harmonic position. The solid line (——) represents the best fit of the data to the model of the surface described by Eq. (3). The line (· · · ·) represents the best fit of the data to the models of the surface described by Eq. (9). The line (— — —) illustrates the best fit for the model described by Eq. (3) to data limited to the range $Q_z \leq 0.3$ Å^{-1}.

of the first peak (approximately 12 Å) is just about equal to the length of the CsPFO molecule, 12.4 Å,[14] and is about half that of the subsequent peaks (approximately 28 Å). This implies that the surface is coated with a monolayer of CsPFO, while the thickness of the layers below the surface is comparable to that of bilayers. The fact that the peak electron density at the surface is very close to that of the neat fluorocarbon polymer Teflon, while that of the first minimum is close to the electron density H_2O, suggests that the surface consists of a relatively dense surfactant monolayer.[33]

In principle, additional data at larger Q_z should improve the spatial resolution of the real-space profile. Figure 9 shows $R(Q_z)/R_F(Q_z)$ data for CsPFO at $T-T_{N-\text{Sm-}A}\cong 1.6\,^\circ$C, which were collected in order to show the structure at the third-harmonic position. The solid line in Fig. 9 illustrates the best fit that we were able to obtain using Eq. (8) and the full range of the data. Agreement with the main peak at $Q_z\cong 0.125$ Å^{-1} is satisfactory, but shapes obtained from the model for the structure at the second- and third-harmonic positions deviate from the data. This discrepancy might be a consequence of the assumption that the form factor is the same for all layers. Additionally, since the surface would be expected to reduce the mean-square fluctuations in the layer position $\langle u^2\rangle$, there should be a depth-dependent Debye-Waller factor, which we did not include in the analysis.

As we mentioned above, the fit that gives rise to this particular real space profile is not unique. In order to determine which features of the real-space density are not sensitive to details of the model, the data were also modeled by the following form, which allows the correlation lengths for the harmonics to differ:

$$\left.\frac{\langle\rho(z)\rangle}{\rho_\infty}\right|_L = \sum_{n=1}^{3} B_n \sin\left[\frac{2\pi(z-z_n)}{L_n}\right]\exp(-z/\xi_n)\,. \quad (9)$$

An analysis of the data with all 12 of the parameters free suggests that $L_1=L_2=L_3$ and $z_1=z_2=z_3$. We therefore fit the data while imposing $L_1=L_2=L_3$ and $z_1=z_2=z_3$, which reduces the number of parameters by 4 and clearly shows that $\xi_1>\xi_2>\xi_3$. The dotted line in Fig. 9 illustrates the best fit obtained using this form and the real-space density corresponding to this model, Eq. (9). The solid and dashed lines in Fig. 9 indicate the best fits obtained using Eq. (8) and employing the full range of data and only $Q_z<0.3$ Å^{-1}, respectively. The real-space densities corresponding to these two models are illustrated by the solid and dashed lines, respectively, in Fig. 10 and the dotted line is the real space density corresponding to the fit using Eq. (9). We believe that the difference between these curves represents the uncertainty in the conclusions that we can draw about the electron density in the real-space surface profile.

For all three fits, the width of the local maximum in the electron density at the surface is approximately half the width of the interior local maxima, as would be expected for a surface monolayer of CsPFO. We believe that almost any model chosen to represent the data would indicate this feature. The minimum electron density for all of visible oscillations to be close to the value for H_2O in all three fits. This suggests that the CsPFO layers are well defined and separated by layers of relatively pure H_2O. However, since the amplitude of the minimum electron density obtained from the model based on Eq. (9) is slightly larger than the density for pure H_2O,

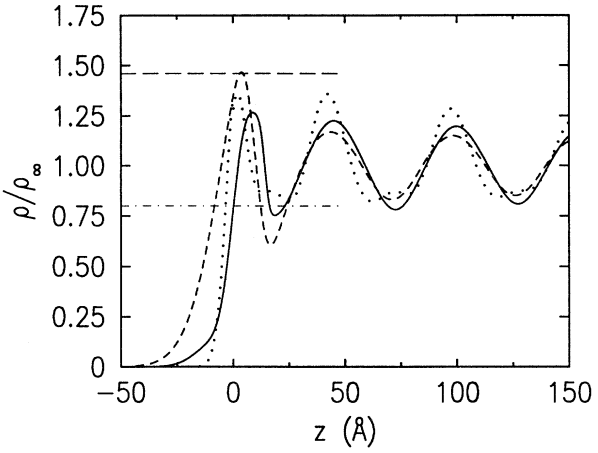

FIG. 10. The electron density profile $\langle\rho(z)\rangle/\rho_\infty$ obtained from fitting the data in Fig. 9. The solid (——) and dashed (— — —) lines correspond to the model described by Eq. (3) for fits that include all of the data, and only data, for $Q_z \leq 0.3$ Å^{-1}, respectively. The dotted line (· · · ·) represents the profile for the model described by Eq. (9). The horizontal lines indicate at 1.46 the electron density of Teflon, and at 0.80, the electron density of H_2O.

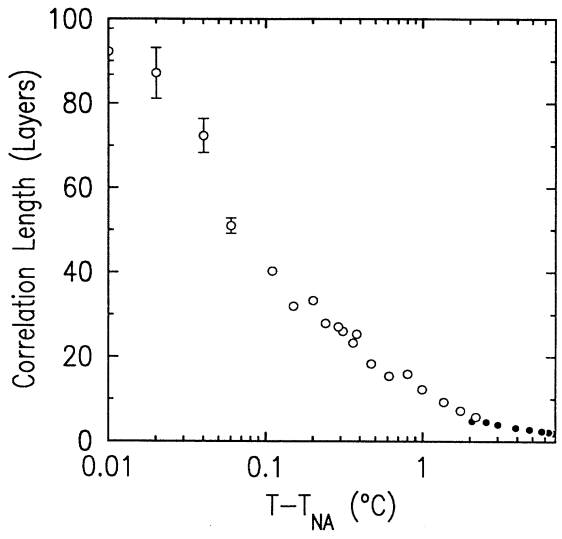

FIG. 11. Temperature dependence of the surface penetration length ξ for two solutions of CsPFO. The values indicated by solid circles (●) correspond to the data displayed in Fig. 4 which $T_{N-\text{Sm-}A}=28$ °C; the values indicated by open circles (○) correspond to data from a sample containing slightly more H_2O in which $T_{N-\text{Sm-}A}=33.2$ °C.

we cannot rule out some small interpenetration of the CsPFO into the water layer. The peak in the electron density of the surface layer is somewhere between $1.28\rho_\infty$ and the density of the bulk fluorocarbon Teflon, approximately equal to $1.43\rho_\infty$. We do not know what density to expect for a fully formed layer of CsPFO, but on the basis of the fact that CsPFO is a strong surfactant we think it reasonable to conclude that the surface is a relatively dense monolayer. If this is the case, then considering that all three models result in approximately the same peak electron densities for the surface monolayer and the near surface bilayers, we believe that the latter are relatively well-formed bilayers rather than smectic arrays of micelles.

In addition, since the near surface profiles (Fig. 8) obtained from the fits shown in Fig. 4 are nearly identical, we conclude that the near-surface smectic order is not very sensitive to the occurrence of the isotropic-to-nematic phase transition in the bulk. The surface penetration lengths ξ, Eq. (4), and ξ_1, Eq. (9), are essentially identical and we believe these values are independent of the model. The temperature dependence of the correlation lengths corresponding to the all of the fits in Fig. 4 are plotted in Fig. 11 as solid dots. There is a systematic increase with decreasing temperature, but it is not very dramatic since the lowest temperature in this data set is about 2 °C above $T_{N-\text{Sm-}A}$.

We obtained more information on the penetration lengths from a separate sample which contained slightly more H_2O; in this sample $T_{N-\text{Sm-}A}\cong 33.2$ °C. The open circles in Fig. 11 illustrate the temperature dependence of ξ extracted from specular reflectivity data over a narrow range of Q_z. The critical nature of this transition is clearly illustrated by the fact that, for the lowest temperature scan ($T=32.93$ °C), the principal peak is at least ten times sharper than the sharpest peak shown in Fig. 4. The data are consistent with a form like $Q_0\xi \sim t^{-2/3}$ where $t\equiv(T/T_{N-\text{Sm-}A}-1)$; however, in view of the problems with slight evaporation, $T_{N-\text{Sm-}A}$ was not well determined and the errors on the exponent can be as large as ± 0.2.

ANALYSIS OF BULK DIFFUSE SCATTERING

As shown by Figs. 5 and 6, the bulk diffuse scattering from the nematic phase of CsPFO-H_2O solutions is qualitatively different from that from thermotropic nematic materials. Nevertheless, we attempted to analyze the data in terms of a model in which the fluctuations could be described by the convolution of the usual anisotropic Lorentzian

$$S_0(\mathbf{Q}-Q_0\hat{\mathbf{n}})=\frac{1}{1+\xi_\parallel^2(\mathbf{Q}\cdot\hat{\mathbf{n}}-Q_0)^2+\xi_\perp^2|\mathbf{Q}\times\hat{\mathbf{n}}|^2}$$

and a Gaussian director distribution function

$$G(\Omega)d\Omega=\left[2\pi\int_0^\pi \exp\left[\frac{-\theta^2}{2\sigma_n^2}\right]\sin(\theta)d\theta\right]^{-1}\times\exp(-\theta^2/2\sigma_n^2)\sin(\theta)d\theta\,d\phi\ , \quad (10)$$

$$S(\mathbf{Q})=\int d\Omega\, S_0(\mathbf{Q}-Q_0\hat{\mathbf{n}})G(\Omega)\ .$$

The effects of the reflectometer resolution were also included in the analysis. In this model, condensation of the diffuse scattering around the point $Q_z\approx 0.125$ Å^{-1} as

$T \rightarrow T_{N-\text{Sm-}A}$ could be reflected in both a decrease of the parameter σ_n, representing the width of the arc scan, and increases in the correlation lengths $\xi_\parallel$ and $\xi_\perp$.

Figure 12 illustrates a fit of this model to data for $T = 32.8\,^\circ\text{C}$. In order to simultaneously display the fits for the radial scans at $\chi = 15°$ and 30°, the data are plotted as a function of Q_x. Table II lists σ_n and the correlation lengths $\xi_\parallel$ and $\xi_\perp$ obtained from fits for two sample temperatures and compares them with the penetration lengths ξ obtained from the specular reflectivity for the same sample.[34] Surprisingly, the bulk correlation lengths obtained from these fits are nearly twice as large as the surface penetration lengths in contrast to the case for thermotropic systems for which the two lengths are typically equal.[17] Theoretically, the surface-induced smectic order must penetrate into the bulk a distance that is equal to or greater than the bulk length,[35] and the discrepancy is most likely a manifestation of the model. For example, although the longitudinal bulk correlation length $\xi_\parallel$ is greater than the surface penetration length ξ, the measured half widths of the radial bulk diffuse scans are equal to, or greater than, the widths of the surface peak. Therefore, the fact that the fit values of $\xi_\parallel$ are larger than the surface values for ξ is probably an artifact of the Gaussian broadening of the Lorentzian form for $S_0(\mathbf{Q}-Q_0\hat{\mathbf{n}})$. The model predicts that the peak of a radial scan is broadened by some weighted average of the term $\xi_\perp^2|\mathbf{Q}\times\hat{\mathbf{n}}|^2$ in the denominator of Eq. (10) and that the fitting procedure drives $\xi_\parallel$ to larger values in order to reduce the calculated half width. For example, the solid line in Fig. 13 illustrates the best fit to data from an os scan [see Fig. 5(b)] at $T = 30.1\,^\circ\text{C}$ using the above model

TABLE II. Typical parameters obtained from the best fits of the model described by Eq. (10) to the bulk diffuse scattering. The last column corresponds to the surface penetration length.

T (°C)	σ_n (deg)	$Q_0\xi_\parallel$	$Q_0\xi_\perp$	$Q_0\xi$
32.1	40	29.1	9.5	16.2
30.1	30	65.1	22.1	26.3

when the Gaussian smearing is neglected, i.e., σ_n is forced to be 0. The fit is not as good as that obtained when σ_n is allowed to vary, but the resulting parameter $Q_0\xi_\parallel = 18.5$ is shorter than the surface length, corresponding to the fact that the half width of the bulk scan is actually broader than that of the specular reflectivity. This value should be compared to $Q_0\xi_\parallel = 65.1$, which is obtained when σ_n is allowed to vary. The effect of the Gaussian broadening is illustrated by the dashed line in Fig. 13, which shows the result from the same model when $\sigma_n = 30°$ and $Q_0\xi_\parallel = 18.5$.

Since the anisotropic Lorentzian model, averaged over an angular distribution of $\hat{\mathbf{n}}$, is inconsistent with theoretical models relating the surface penetration depth to the bulk correlation length, and in the absence of theoretical guidance, we considered the simplest generalization of this model by adding terms with higher powers of $|\mathbf{Q}\times\hat{\mathbf{n}}|^2$ to the denominator of Eq. (10). In fact, terms of order $(|\mathbf{Q}\times\hat{\mathbf{n}}|^2)^2$ do improve the quality of the fits to critical scattering from thermotropic systems.[28] Fits to any functional form for S_0 that falls off sufficiently faster than $1/|\mathbf{Q}\times\hat{\mathbf{n}}|^2$ will probably allow a satisfactory fit with shorter values for $Q_0\xi_\parallel$, even when convolved with a Gaussian.

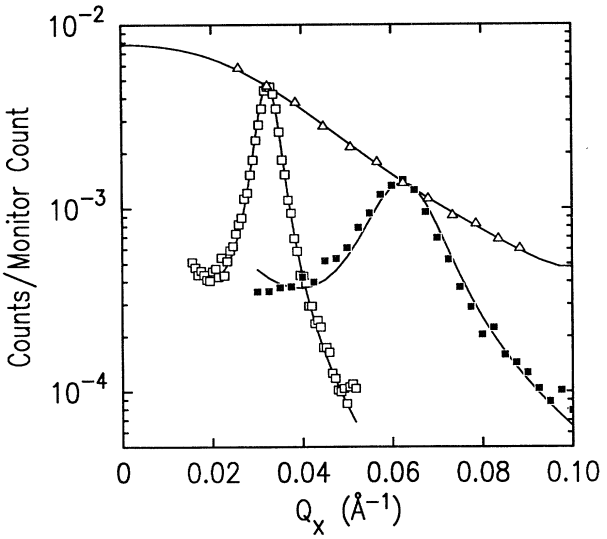

FIG. 12. Diffuse scattering as a function of Q_x from the bulk of a CsPFO solution containing 58% H_2O by weight at T=31.0°C. The scans are as follows: arc scan at $|\mathbf{Q}| = Q_0$ and $Q_y \approx 6\times10^{-4}$ Å^{-1} (△), and radial scans at 15° (□) and 30° (■). The solid lines are fits to the model of Eq. (10).

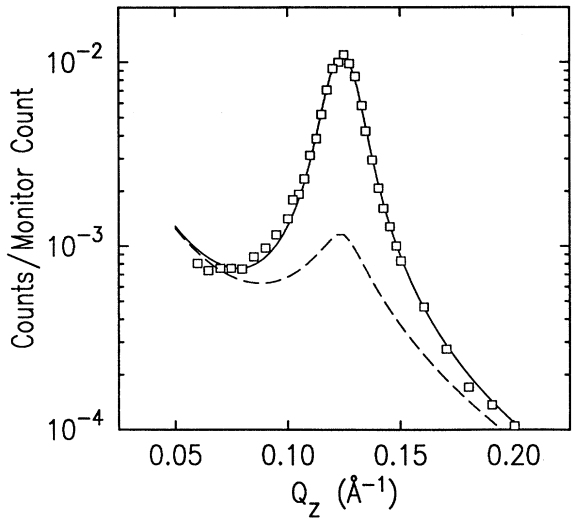

FIG. 13. The solid line (——) is the best fit of an anisotropic Lorentzian model, Eq. (10), to the bulk diffuse scattering data (□) at the peak of the os scan [see Fig. 5(b)] for $Q_x \approx Q_y \approx 0$ assuming no angular distribution of $\hat{\mathbf{n}}$. The dashed line (— — —) uses the same correlation lengths as the solid line, except that the Gaussian width of the distribution for $\hat{\mathbf{n}}$ is taken to be 30°.

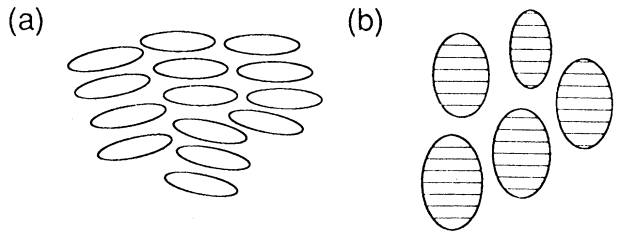

FIG. 14. (a) A possible model for the critical smectic fluctuations in the nematic phase of a micellar nematic phase. (b) Duplication of the sketch presented by de Gennes representing regions of smectic-A fluctuations, i.e., "cybotactic groups" in thermotropic nematic phases.

Figure 14(a) illustrates one possible physical model that would explain the observed properties of the thermal diffuse scattering. Since the thickness of the micelles is primarily determined by the length of the CsPFO molecule, this parameter cannot vary much between micelles. Similarly, as the space between micelles is also not likely to vary much, there is certain to be a peak at $2\pi/D$, where D is the micelle-micelle distance along the normal to the broad surface. The diffuse scattering indicates a Gaussian-like distribution of this direction. On the other hand, the data require that the scattering from any domain decrease faster than a $1/q^2$ power law in the directions transverse to the local director. Furthermore, since this fact is true at the highest temperatures, it cannot be explained by a temperature-induced increase in the lateral size of the micelles. One possibility is that there is a significant inhomogeneity in either the lateral dimensions of the micelles or the intermicellar distance. Gaussian statistics for either of these variables would give rise to a Gaussian decrease in the scattering transverse to the local direction. This is qualitatively different from the generally accepted picture of critical smectic fluctuations in thermotropic systems [Fig. 14(b)] in which the director fluctuations are less important and the transverse correlation function decrease is much closer to being exponential.[36]

SUMMARY

The main purpose of this paper has been to demonstrate the use of the reflection geometry to study the free surface of the lyotropic liquid-crystal CsPFO-H_2O system. We have demonstrated that the free surface induces smectic order at temperatures from which the bulk phase is either isotropic or nematic. Although the surface-induced order is insensitive to the isotropic to nematic transition, its penetration into the bulk nematic phase increases dramatically as the temperature approaches the nematic–to–smectic-A transition. Technical difficulties associated with maintaining the H_2O concentration were responsible for variations in $T_{N-\mathrm{Sm}\text{-}A}$ that restricted our ability to make high-precision critical measurements. Nevertheless, we were able to demonstrate smectic wetting of the nematic surface to approximately 100 layers.

The observed specular reflectivity can be described by models for the electron density that assume a surface monolayer of CsPFO, followed by a layer of nearly pure H_2O. Data taken at the largest angles, and consequently with the highest resolution, indicate that the electron densities of the subsurface bilayers are comparable to that of the surface monolayer. Since it is likely that the surface for such high concentrations of CsPFO is a uniform monolayer, the fact that the peak electron densities of the subsurface bilayers in the model profiles are so close to that of the surfactant monolayer effectively excludes the possibility that the subsurface bilayers are planar arrays of loosely packed micelles.

Since surface-induced smectic order induces bulk orientational order in the nematic phase, we were able to study diffuse x-ray scattering from critical smectic fluctuations in a well-oriented lyotropic nematic phase. The principal result was the demonstration that the scattering is qualitatively different from that of thermotropic systems.

The major limitation to this study was the difficulty in maintaining the chemical composition of the CsPFO-H_2O solutions. This was principally caused by the large free volume of our sample cell. Alternative systems, such as one in which the chemical potential of the H_2O is maintained, should be considered;[14,37] however, the amount of time necessary to achieve equilibrium could be unacceptably long. Other geometries with little or no free volume in which one studies the order induced by a solid surface might be practical; but there are other technical problems there, too. These technical difficulties aside, it would be interesting to carry out studies similar to those presented here on other lyotropic systems.

ACKNOWLEDGMENTS

This work was supported by the National Science Foundation (NSF) through a grant to the Harvard Materials Research Laboratory, No. NSF-DMR-89-20490, and NSF Grant No. DMR-88-12855-925-7996. Two of us (J.D.L. and G.S.) were supported, in part, by NSF Grant No. DMR-86-19234. Research carried out at the National Synchrotron Light Source, Brookhaven National Laboratory, is supported by the Department of Energy, Material Sciences and Division of Chemical Sciences under Contract No. DE-AC02-76CH00016.

*Present address: Department of Physics, Brookhaven National Laboratory, Upton, NY 11973.

[1]P. G. de Gennes, *The Physics of Liquid Crystals* (Clarendon, Oxford, 1974).

[2]P. S. Pershan, *The Structure of Liquid Crystal Phases* (World Scientific, Singapore, 1988).

[3]P. G. de Gennes, Solid State Commun. **10**, 753 (1972).

[4]T. C. Lubensky, J. Chim. Phys. **80**, 31 (1983).

[5]See, for example, *Physics of Complex and Supermolecular Fluids,* edited by S. A. Safran and N. A. Clark (Wiley, New York, 1987).

[6]*Physics of Amphiphiles-Micelles, Vesicles and Microemulsions,* Proceedings of the International School of Physics "Enrico Fermi," Course XC, edited by V. Degiorgio and M. Corti (North-Holland, Amsterdam, 1985).

[7]G. S. Smith, E. B. Sirota, C. R. Safinya, and N. A. Clark, Phys. Rev. Lett. **60**, 813 (1988).

[8]C. R. Safinya, E. B. Sirota, D. Roux, and G. S. Smith, Phys. Rev. Lett. **62**, 1134 (1989).

[9]N. Boden, P. H. Jackson, K. McMullen, and M. C. Holmes, Chem. Phys. Lett. **65**, 476 (1979).

[10]N. Boden and M. C. Holmes, Chem. Phys. Lett. **109**, 76 (1984).

[11]N. Boden, K. McMullen, and M. C. Holmes, in *Magnetic Resonance in Colloid and Interface Science,* edited by J. P. Fraissard and H. A. Resing (Reidel, Dordrecht, 1980), p. 667.

[12]C. Rosenblatt, S. Kumar, and J. D. Litster, Phys. Rev. A **29**, 1010 (1984); M. R. Fisch, S. Kumar, and J. D. Litster, Phys. Rev. Lett. **57**, 2830 (1986); B. D. Larson and J. D. Litster, Mol. Cryst. Liq. Cryst. **113**, 13 (1984).

[13]C. Rosenblatt, Phys. Rev. A **32**, 115 (1985).

[14]N. Boden, S. A. Corne, M. C. Holmes, P. H. Jackson, D. Parker, and K. W. Jolley, J. Phys. (Paris) **47**, 2135 (1986).

[15]B. M. Ocko, R. J. Birgeneau, and J. D. Litster, Z. Phys. B **62**, 487 (1986).

[16]P. S. Pershan and J. Als-Nielsen, Phys. Rev. Lett. **52**, 759 (1984).

[17]P. S. Pershan, A. Braslau, A. H. Weiss, and J. Als-Nielsen, Phys. Rev. A **35**, 4800 (1987).

[18]B. M. Ocko, A. Braslau, P. S. Pershan, and J. Als-Nielsen, Phys. Rev. Lett. **57**, 94 (1986).

[19]If the transition were second order the smectic phase would "critically wet" the free surface and the number of layers would diverge. Unfortunately, we were not able to work sufficiently close to $T_{N-\mathrm{Sm}\text{-}A}$ to verify "critical wetting."

[20]The x-ray measurement required thin flat samples with relatively large surface-to-volume ratios. See Ref. 17.

[21]J. Als-Nielsen and P. S. Pershan, Nucl. Instrum. Methods **208**, 545 (1983).

[22]P. S. Pershan, J. Phys. (Paris) Colloq. **50**, C7-1 (1989).

[23]In order to ensure that the incident beam always strikes the same point, the sample must also be translated horizontally transverse to L.

[24]Neglecting absorption effects $R_F(Q_z)=[s^2+(s-1)^{1/2}]^4$, where $s\equiv Q_z/Q_c$. The "critical wave vector" $Q_c=\sqrt{16\pi\rho r_0}$, where ρ is the average electron density of the bulk solution and r_0 is the classical radius of the electron. For the 58 wt. % H_2O solution of CsPFO $Q_c=0.024$ Å^{-1}.

[25]We were not able to make accurate measurements very close to the transition temperature since, on cooling through $T_{N-\mathrm{Sm}\text{-}A}$ the sample would undergo changes which we attributed to the loss of H_2O. This made it impossible to measure $T_{N-\mathrm{Sm}\text{-}A}$ by cycling back and forth through the transition in small temperature intervals. The sample behavior was completely reversible if it was heated up to the isotropic phase and recooled, as long as it remained in the nematic phase. Since equilibrium obtained by this procedure took approximately 2 h it was not practical to do it repeatedly.

[26]The only exceptions are those thermotropic systems for which there is competition between layering at D and $2D$. See, for example, P. S. Pershan, *The Structure of Liquid Crystal Phases* (World Scientific, Singapore, 1988).

[27]E. F. Gramsbergen, W. H. de Jeu, and J. Als-Nielsen, J. Phys. (Paris) **47**, 711 (1986); E. F. Gramsbergen and W. H. de Jeu, *ibid.* **49**, 363 (1988).

[28]W. L. McMillan, Phys. Rev. A **7**, 119 (1973).

[29]See, for example, A. De Vries, Mol. Cryst. Liq. Cryst. **10**, 219 (1970).

[30]A. Braslau, P. S. Pershan, G. Swislow, B. M. Ocko, and J. Als-Nielsen, Phys. Rev. A **38**, 2457 (1988).

[31]The parameters for these fits are listed in Table I.

[32]The average electron density for the CsPFO solution containing 58% H_2O by weight is 0.42 electrons Å^{-3}. For H_2O the electron density is 0.33 electron Å^{-3} and for solid Teflon it is 0.60 electrons Å^{-3}.

[33]The electron density of solid Teflon is approximately 1.8 times the electron density of H_2O.

[34]Since the bulk resolution is comparable to the widths observed at the lowest temperatures, the parameters for those temperatures are not reported. Nevertheless, for all temperatures the extracted values for $\xi_{\|}$ are approximately a factor of 2 larger than those of the surface penetration length ξ.

[35]See, for example, P. G. de Gennes, Rev. Mod. Phys. **57**, 827 (1985).

[36]See, for example, Fig. 5a of P. G. de Gennes, Mol. Cryst. Liq. Cryst. **21**, 49 (1973).

[37]P. S. Pershan, J. Phys (Paris) Colloq. **4**, C3-423, (1979).